

Matrix-Response Generalized Linear Mixed Model with Applications to Longitudinal Brain Images

Zhentao Yu, Jiaqi Ding, Guorong Wu, and Quefeng Li

*Department of Biostatistics, Gillings School of Global Public Health,
University of North Carolina at Chapel Hill*

*Department of Computer Science, College of Arts and Sciences,
University of North Carolina at Chapel Hill*

February 4, 2026

Abstract

Longitudinal brain imaging data facilitate the monitoring of structural and functional alterations in individual brains across time, offering essential understanding of dynamic neurobiological mechanisms. Such data improve sensitivity for detecting early biomarkers of disease progression and enhance the evaluation of intervention effects. While recent matrix-response regression models can relate static brain networks to external predictors, there remain few statistical methods for longitudinal brain networks, especially those derived from high-dimensional imaging data. We introduce a matrix-response generalized linear mixed model that accommodates longitudinal brain networks and identifies edges whose connectivity is influenced by external predictors. An efficient Monte Carlo Expectation–Maximization algorithm is developed for parameter estimation. Extensive simulations demonstrate effective identification of covariate-related network components and accurate parameter estimation. We further demonstrate the usage of the proposed method through applications to diffusion tensor imaging (DTI) and functional MRI (fMRI) datasets.

Keywords: EM algorithm, Generalized Linear Mixed Model, Longitudinal data, Low rank matrix, Sparsity.

1 Introduction

The Human Connectome Project (HCP) is a large-scale international effort to map the structural and functional connectivity networks of the human brain. Network models are widely used in brain connectivity research (Bassett *and others*, 2018). Such studies acquire multimodal neuroimaging data—including Magnetic Resonance Imaging (MRI), Positron Emission Tomography (PET), and Diffusion Tensor Imaging (DTI)—from multiple subjects to characterize the brain’s functional and structural organization (Babaeeghazvini *and others*, 2021). For each subject, these data can be used to construct a connectivity network, with nodes representing regions of interest (ROIs) and edges encoding functional or structural relationships between regions. Alterations in these networks are associated with neurodegenerative disorders, including Alzheimer’s disease, Lewy body dementia, and Parkinson’s disease. A central challenge in neuroscience is to identify biomarkers that capture or predict network changes, enabling earlier diagnosis and intervention. The recent emergence of large imaging data consortia, such as ADNI (<https://adni.loni.usc.edu>) and UK Biobank (<https://www.ukbiobank.ac.uk/>), has given researchers access to large-scale longitudinal brain-imaging datasets, which are preferable to traditional cross-sectional snapshots acquired at a single time point. These longitudinal datasets are invaluable for detecting age-related cognitive decline, tracking the progression of neurodegenerative diseases, mapping the development of brain function in youth, and addressing numerous other key questions in neuroscience.

Generalized linear mixed models (GLMMs) are widely used for longitudinal data. In GLMMs, fixed effects capture population-level trends, whereas random effects account for between-subject variability. However, standard GLMMs do not directly accommodate matrix-valued responses and thus cannot be used to relate brain networks to external predictors. Recent advances in matrix-response regression address this limitation. Zhang *and others* (2023) proposed matrix-response generalized linear models for cross-sectional brain images, extending traditional generalized linear models to matrix-valued responses and showing that, by exploiting low-rank and sparse structures in the coefficient matrices, their estimators are consistent; they also demonstrated superior empirical performance over methods that ignore matrix structure. Zhou and Mueller (2022) developed graph Laplacian regression models that perform local smoothing on graph Laplacians. While applicable to brain networks, their methods target a specialized class (graph Laplacians) rather than general network matrices. Moreover, neither of the above methods handles longitudinal imaging data. Zhao *and others* (2024) proposed a longitudinal regression model for covariance-matrix outcomes. Although it accommodates longitudinal imaging data, the response is a scalar derived from eigenpairs of covariance matrices rather than a general matrix. Consequently, it cannot directly identify features that drive changes in whole-brain network structure. More details of these existing methods can be found in Section 2.3.

In this article, we introduce a class of matrix-response generalized linear mixed models (MR-GLMMs) for longitudinal brain networks, where responses are time-indexed square matrices. We assume that after transformation of canonical link functions, their conditional means can be written as a linear combination of time-varying covariates with matrix-valued

coefficients plus a matrix-valued intercept that accommodates random effects. We assume that the matrix-intercept term is low-rank and the matrix-coefficients are sparse. Then, we propose to solve a constrained likelihood maximization problem to obtain estimators of parameters of MR-GLMMs. The main challenge is that the likelihood function involves evaluating high-dimensional integrals, which are computationally challenging. To address this, we develop an efficient Monte Carlo Expectation–Maximization (MCEM) algorithm to compute the estimators. In the E-step, we employ Metropolis-within-Gibbs (MwG) schemes previously developed in Heiling *and others* (2024) to approximate the required integrals. We conduct extensive simulations to evaluate variable selection and estimation accuracy of our method and compare it against element-wise penalized GLMMs. Across scenarios, our approach consistently outperforms these alternatives. We further analyze two longitudinal neuroimaging datasets, illustrating the model’s ability to identify key biomarkers.

The rest of the paper is organized as follows. In Section 2, we introduce the proposed MR-GLMM and compare it with other matrix-response regression models in the literature. In Section 3, we amplify the details of the Monte Carlo Expectation-Maximization algorithm for solving parameters in our proposed model and tuning parameter selections. Our method’s effectiveness is demonstrated in Section 4 through extensive simulation studies comparing with the element-wise penalized GLMM approaches across various scenarios. In Section 5, we apply our method to two real-world neuroimaging datasets: a DTI dataset from ADNI examining age, sex, APOE4, and diagnostic status effects on structural connectivity, and a fMRI dataset from the HCP investigating task-induced changes in resting-state networks.

2 Matrix Response Generalized Linear Mixed Model

2.1 Notation

For a matrix $\mathbf{A} \in \mathbb{R}^{d_1 \times d_2}$, let \mathbf{A}_{ij} denote the (i, j) -th element, and let $\mathbf{A}_{i\cdot}$ and $\mathbf{A}_{\cdot j}$ represent its i -th row and j -th column, respectively. Let $\|\mathbf{A}\|_2 = \lambda_{\max}(\sqrt{\mathbf{A}^\top \mathbf{A}})$ and $\|\mathbf{A}\|_F = \sqrt{\sum_{i,j} |\mathbf{A}_{ij}|^2}$ denote the L_2 and Frobenius norms of \mathbf{A} . Let $\text{SVD}_r(\mathbf{A}) = [\mathbf{U}, \mathbf{\Sigma}, \mathbf{V}]$ denote the rank- r truncated Singular Value Decomposition (SVD) of matrix \mathbf{A} such that $\mathbf{A} = \mathbf{U}\mathbf{\Sigma}\mathbf{V}^\top$, where $\mathbf{\Sigma} \in \mathbb{R}^{r \times r}$ is a diagonal matrix containing the r largest singular values of \mathbf{A} , and $\mathbf{U} \in \mathbb{R}^{d_1 \times r}$, $\mathbf{V} \in \mathbb{R}^{d_2 \times r}$ contain the corresponding left and right singular vectors, respectively. For a tensor $\mathcal{B} \in \mathbb{R}^{d_1 \times d_2 \times d_3}$, let $\mathcal{B}_{i,j,k}$ denote its (i, j, k) -th entry, $\mathcal{B}_{i,j,\cdot}$ denote the (i, j) -th tube fiber, and $\mathcal{B}_{\cdot,\cdot,k}$ denote the k -th frontal slice of \mathcal{B} . Let $\|\mathcal{B}\|_F = \sqrt{\sum_{ijk} \mathcal{B}_{ijk}^2}$ denote its Frobenius norm and $\|\mathcal{B}\|_0$ denote the number of nonzero elements in \mathcal{B} .

2.2 Model Settings

For a sample of N individuals, suppose we observe independent longitudinal network data represented by adjacency matrices $\mathbf{A}_{it} \in \mathbb{R}^{n \times n}$, where $1 \leq i \leq N$ indexes the subjects and $1 \leq t \leq T_i$ denotes the time points, with T_i being the number of observations for subject i .

Each $n \times n$ adjacency matrix represents a network with n nodes. Additionally, we observe time-varying covariates $\mathbf{x}_{it} = (x_{it1}, \dots, x_{itp})^\top \in \mathbb{R}^p$ for each individual. We assume that, conditional on \mathbf{x}_{it} , the adjacency matrix \mathbf{A}_{it} follows a multiplicative exponential family distribution with a canonical link function, whose density function has the form

$$f(\mathbf{A}_{it}|\mathbf{x}_{it}) = \prod_{j \neq j'}^n h(A_{it,jj'}) \exp(A_{it,jj'}\eta_{it,jj'} - \psi(\eta_{it,jj'})),$$

where $\eta_{it,jj'}$ is the (j, j') -th element of $\boldsymbol{\eta}_{it} = g(\boldsymbol{\mu}_{it})$, $\boldsymbol{\mu}_{it} = \mathbb{E}(\mathbf{A}_{it}|\mathbf{x}_{it})$, $g(\cdot)$ is a commonly-used link function in GLM applied element-wise, and $\psi(\cdot)$ is the cumulant function satisfying $\psi'(\cdot) = g^{-1}(\cdot)$. We assume that the link function takes the form

$$g(\boldsymbol{\mu}_{it}) = \boldsymbol{\Theta} + \boldsymbol{\theta}_i + \mathcal{B} \times_3 \mathbf{x}_{it}, \quad (1)$$

where $\boldsymbol{\Theta} \in \mathbb{R}^{n \times n}$ is the fixed intercept matrix that characterizes the population-level connectivity, $\boldsymbol{\theta}_i \in \mathbb{R}^{n \times n}$ is the random intercept matrix for subject i , and each element $\theta_{i,jk}$ is assumed to follow $\mathcal{N}(0, \sigma_{\theta,jk}^2)$. We define $\boldsymbol{\Sigma}_\theta \in \mathbb{R}^{n \times n}$ as the matrix of variances where $[\boldsymbol{\Sigma}_\theta]_{jk} = \sigma_{\theta,jk}^2$, and $\mathcal{B} \in \mathbb{R}^{n \times n \times p}$ as the slope tensor that defines the effects of covariates on the connectivity matrix, and $\mathcal{B} \times_3 \mathbf{x}_{it} = \sum_{l=1}^p x_{itl} \mathcal{B}_{::,l}$, where x_{itl} is the l -th element of \mathbf{x}_{it} . We assume that the population-level connectivity matrix $\boldsymbol{\Theta}$ has a low-rank structure, a common assumption in brain network modeling (Zhang *and others*, 2023). Under this assumption, we perform the Burer-Monteiro factorization of $\boldsymbol{\Theta}$ by writing it as $\boldsymbol{\Theta} = \mathbf{U}\mathbf{V}^\top$ (Burer and Monteiro, 2003), where $\mathbf{U}, \mathbf{V} \in \mathbb{R}^{n \times r}$ and r denotes the rank of $\boldsymbol{\Theta}$. This reparameterization eliminates the need for computationally expensive SVD calculations at each iteration and represents a standard approach in optimization literature for enforcing low-rank constraints. Furthermore, we assume that \mathcal{B} is exactly sparse in the sense that many of its elements are exactly zero. This sparsity assumption posits that covariate effects are confined to specific subsets of connections, consistent with findings from empirical neuroscience research. Then, the parameters of interests are $\boldsymbol{\vartheta} = (\mathbf{U}, \mathbf{V}, \mathcal{B})$. We denote $\ell(\boldsymbol{\theta})$ as the observed marginal full log-likelihood of the form

$$l(\boldsymbol{\vartheta}) = \sum_{i=1}^N \log \int f(\mathbf{A}_i|\mathbf{x}_i, \boldsymbol{\theta}_i; \boldsymbol{\vartheta}) \phi(\boldsymbol{\theta}_i) d\boldsymbol{\theta}_i, \quad (2)$$

where $f(\mathbf{A}_i|\mathbf{x}_i, \boldsymbol{\theta}_i; \boldsymbol{\vartheta}) = \prod_{t=1}^{T_i} f(\mathbf{A}_{it}|\mathbf{x}_{it}, \boldsymbol{\theta}_i; \boldsymbol{\vartheta})$, and $\phi(\boldsymbol{\theta}_i)$ denotes the normal density of $\boldsymbol{\theta}_i$. To estimate $\boldsymbol{\vartheta}$, we propose to solve the following optimization problem:

$$\min_{\boldsymbol{\vartheta}} -l(\boldsymbol{\vartheta}) + \gamma \|\mathbf{U}^\top \mathbf{U} - \mathbf{V}^\top \mathbf{V}\|_F^2, \text{ subject to } \|\mathcal{B}\|_0 \leq sn^2, \quad (3)$$

where γ and s are two positive tuning parameters. In (3), we incorporate a regularization term $\|\mathbf{U}^\top \mathbf{U} - \mathbf{V}^\top \mathbf{V}\|_F^2$ to enforce uniqueness in the factorization $\boldsymbol{\Theta} = \mathbf{U}\mathbf{V}^\top$, a technique also employed in other neuroimaging approaches (Zhang *and others*, 2023). Moreover, we add the constraint $\|\mathcal{B}\|_0 \leq sn^2$ to ensure rendering a sparse estimator of \mathcal{B} . The L_0 -constraint is known to introduce less bias into the estimator compared to other constraints, such as the L_1 -constraint.

2.3 Existing Matrix-response Regression Models

Zhang *and others* (2023) proposed cross-sectional matrix-response generalized linear models for studying brain networks. Their model assumes that $\{\mathbf{A}_i\}_{i=1}^N$ are i.i.d. networks represented by $n \times n$ matrices, where $\mathbf{A}_i \in \mathbb{R}^{n \times n}$. These networks are regressed on a set of covariates using generalized linear models. Specifically, let $\mathbf{A}_{i,jj'}$ denote the (j, j') -th element of \mathbf{A}_i , and $\mathbf{x}_i \in \mathbb{R}^p$ be the covariate vector. They assume that the conditional density of $\mathbf{A}_i | \mathbf{x}_i$ follows the canonical form of the exponential family:

$$f(\mathbf{A}_i | \mathbf{x}_i) = \prod_{j \neq j'}^n h(\mathbf{A}_{i,jj'}) \exp(\mathbf{A}_{i,jj'} \eta_{i,jj'} - \psi(\eta_{i,jj'})),$$

where $\eta_{jj'}$ is the (j, j') -th element of $\boldsymbol{\eta}_i = g(\boldsymbol{\mu}_i) = \boldsymbol{\Theta} + \sum_{l=1}^p x_{il} \mathcal{B}_{:, :, l}$ that $\boldsymbol{\mu}_i = \mathbb{E}(\mathbf{A}_i | \mathbf{x}_i)$, x_{il} is the l -th element of \mathbf{x}_i and $\mathcal{B}_{:, :, l}$ is the l -th frontal slice of \mathcal{B} , $g(\cdot)$ is the link function, and $\psi'(\cdot) = g(\cdot)^{-1}$. To deal with high-dimensional networks, they assumed that $\boldsymbol{\Theta}$ is low-rank and \mathcal{B} is sparse. Then, they proposed to solve a penalized GLM problem by imposing a low-rank decomposition on $\boldsymbol{\Theta}$ and sparsity-induced penalty on \mathcal{B} . They showed that the resulting estimators have desirable statistical properties and satisfactory numerical performance through extensive numerical studies. Their method is applicable to study cross-sectional brain networks. However, their method is not applicable for longitudinal brain networks, which are the main objects of interest of our proposed method.

Zhou and Mueller (2022) considered cross-sectional graph Laplacian regression models. For a graph with n nodes and bounded non-negative edge weights w_{ij} , its graph Laplacian is defined as $\mathbf{A} = (a_{ij}) \in \mathbb{R}^{n \times n}$, where $a_{ij} = -w_{ij}$ for $i \neq j$ and $a_{ii} = \sum_{k \neq i} w_{ik}$. Define the space of graph Laplacians as $\mathcal{A}_n = \{\mathbf{A} \in \mathbb{R}^{n \times n} : \mathbf{A} = \mathbf{A}^\top, \mathbf{A} \mathbf{1}_n = \mathbf{0}_n\}$, equipped with a metric

$$d(\mathbf{A}_1, \mathbf{A}_2) = \|\mathbf{A}_1 - \mathbf{A}_2\|_F = \{\text{tr}[(\mathbf{A}_1 - \mathbf{A}_2)^\top (\mathbf{A}_1 - \mathbf{A}_2)]\}^{1/2}.$$

Let $\mathbf{X} \in \mathbb{R}^p$ be the random covariate vector and $\mathbf{x} \in \mathbb{R}^p$ be a deterministic vector. For a graph Laplacian \mathbf{A} , their model aims to find the graph Laplacian that minimizes the conditional Fréchet mean, i.e.,

$$m(\mathbf{x}) = \arg \min_{\boldsymbol{\omega} \in \mathcal{A}_n} \mathbb{E}[d^2(\mathbf{A}, \boldsymbol{\omega}) | \mathbf{X} = \mathbf{x}].$$

They proposed approximating such a conditional mean function using a function that minimizes the weighted squared distance, i.e.,

$$m_G(\mathbf{x}) = \arg \min_{\boldsymbol{\omega} \in \mathcal{A}_n} \mathbb{E}[s_G(\mathbf{x}) d^2(\mathbf{A}, \boldsymbol{\omega})],$$

where $s_G(\mathbf{x}) = 1 + (\mathbf{X} - \boldsymbol{\mu})^\top \boldsymbol{\Sigma}^{-1} (\mathbf{x} - \boldsymbol{\mu})$, $\boldsymbol{\mu} = \mathbb{E}(\mathbf{X})$, and $\boldsymbol{\Sigma} = \text{Var}(\mathbf{X})$. In practice, with i.i.d graph Laplacians $\{\mathbf{A}_i\}_{i=1}^N$, an estimator of $m_G(\mathbf{x})$ can be obtained by solving

$$\hat{m}_G(\mathbf{x}) = \arg \min_{\boldsymbol{\omega} \in \mathcal{A}_n} \frac{1}{N} \sum_{i=1}^N s_G^{(i)}(\mathbf{x}) d^2(\mathbf{A}_i, \boldsymbol{\omega}),$$

where $s_G^{(i)}(\mathbf{x}) = 1 + (\mathbf{X}_i - \bar{\mathbf{X}})^\top \widehat{\boldsymbol{\Sigma}}^{-1}(\mathbf{x} - \bar{\mathbf{X}})$, \mathbf{X}_i is the covariate vector of the i -th subject, $\bar{\mathbf{X}} = N^{-1} \sum_{i=1}^N \mathbf{X}_i$, and $\widehat{\boldsymbol{\Sigma}}$ is the sample covariance of $\boldsymbol{\Sigma}$. When $m(\mathbf{x})$ is a smooth function, they further proposed a locally smoothed estimator by solving

$$\widehat{m}_L(\mathbf{x}) = \arg \min_{\boldsymbol{\omega} \in \mathcal{A}_n} \frac{1}{N} \sum_{i=1}^N s_L^{(i)}(\mathbf{x}, h) d^2(\mathbf{A}_i, \boldsymbol{\omega}),$$

where $\widehat{s}_L^{(i)}(\mathbf{x}, h) = \widehat{\delta}^{-1} [K_h(\mathbf{X}_k - \mathbf{x}) \{1 - (\mathbf{X}_k - \mathbf{x})^\top \widehat{\boldsymbol{\Xi}}^{-1} \widehat{\boldsymbol{\mu}}_1\}]$, $K_h(u) = h^{-1} K(u/h)$ is a kernel function with bandwidth h , $\widehat{\delta} = \widehat{\boldsymbol{\mu}}_0 - \widehat{\boldsymbol{\mu}}_1^\top \widehat{\boldsymbol{\Xi}}^{-1} \widehat{\boldsymbol{\mu}}_1$, and $\widehat{\boldsymbol{\mu}}_0$, $\widehat{\boldsymbol{\mu}}_1$ and $\widehat{\boldsymbol{\mu}}_2$ are moment estimators of $\boldsymbol{\mu}_0 = \mathbb{E}[K_h(\mathbf{X} - \mathbf{x})]$, $\boldsymbol{\mu}_1 = \mathbb{E}[K_h(\mathbf{X} - \mathbf{x})(\mathbf{X} - \mathbf{x})]$, $\boldsymbol{\Xi} = \mathbb{E}[K_h(\mathbf{X} - \mathbf{x})(\mathbf{X} - \mathbf{x})(\mathbf{X} - \mathbf{x})^\top]$, respectively.

Compared with our method, the approach of Zhang *and others* (2023) targets a more specialized class of networks, namely graph Laplacians, whereas our matrix-response model imposes fewer restrictions on network structure. Beyond this scope difference, there are several notable distinctions. First, their method remains a cross-sectional regression model and thus cannot be applied to longitudinal imaging data; it also makes it difficult to accommodate between-subject heterogeneity. Second, their local smoothing approach does not extend well to high-dimensional imaging data, as kernel smoothing is known to suffer from the curse of dimensionality. Finally, although the estimated conditional mean function enables prediction of graph Laplacians, it is less interpretable than our parametric additive model.

Zhao *and others* (2024) developed a longitudinal regression model for analyzing covariance matrix outcomes. The model identifies principal components of covariance matrices that are associated with the covariates, estimate regression coefficients, and discovers within-subject variation in covariance matrices. In particular, they considered longitudinal covariance matrices \mathbf{A}_{it} for $1 \leq i \leq N$ and $1 \leq t \leq T_i$ and proposed the following model:

$$\log(\boldsymbol{\gamma}^\top \mathbf{A}_{it} \boldsymbol{\gamma}) = \beta_0 + u_i + \mathbf{x}_{1i}^\top \boldsymbol{\beta}_1 + \mathbf{x}_{2it}^\top (\boldsymbol{\beta}_2 + \boldsymbol{\nu}_i),$$

where $\boldsymbol{\gamma} \in \mathbb{R}^p$ is the principal component vector, β_0 is the fixed intercept, u_i is the random intercept, \mathbf{x}_{1i} is the time-invariant covariate with a fixed-effect coefficient $\boldsymbol{\beta}_1$, \mathbf{x}_{2it} is the time-varying covariate with random-effect coefficient $\boldsymbol{\beta}_2 + \boldsymbol{\nu}_i$. This model can be regarded as a generalized linear mixed model with a logarithm link function applied to the univariate response $\boldsymbol{\gamma}^\top \mathbf{A}_{it} \boldsymbol{\gamma}$. It aims to find the association between covariates and the covariance matrices. They proposed to obtain estimators of those parameters by maximizing the hierarchical-likelihood function with identifiability constraint. They proved that the resulting estimators are asymptotically consistent and the corresponding covariance matrix estimator is efficient in both low and high-dimensional settings.

Although their model can handle longitudinal brain images, it differs from ours in several fundamental ways. First, in our model (1), the entire matrix serves as the response, and the coefficient tensor $\boldsymbol{\mathcal{B}}$ fully encodes how the covariates influence each matrix entry (i.e., each network edge). By contrast, their model's response is an eigenvalue-based metric rather than the matrix itself. Consequently, the two models are intrinsically different. Moreover, the dimensionality of our model's parameter space is substantially higher than

theirs, posing much greater computational challenges for developing efficient algorithms to solve our problem. In the next section, we give more details of our algorithm.

3 Monte Carlo Expectation Maximization Algorithm

We propose a Monte Carlo Expectation–Maximization (MCEM) algorithm to solve the optimization problem in (3). The observed likelihood function in (2) requires evaluating an expectation with respect to the distribution of $\boldsymbol{\theta}_i$, which is essentially a high-dimensional integration problem and computationally challenging. In the E-step of the algorithm, we propose to approximate the expectation using Monte Carlo sampling approach and minimize the resulting Q-function (Gilks *and others*, 1995) in the subsequent M-step. Then, we iterate between the E-step and M-step.

At the h -th iteration of the MCEM algorithm, the complete log-likelihood function can be written as

$$\begin{aligned} \log(L_c(\mathbf{d}_c; \boldsymbol{\vartheta} | \mathbf{d}_o, \boldsymbol{\vartheta}^{(h)})) &= \log \prod_{i=1}^N f(\mathbf{A}_i, \mathbf{x}_i, \boldsymbol{\theta}_i | \mathbf{d}_o, \boldsymbol{\vartheta}^{(h)}) \phi(\boldsymbol{\theta}_i) \\ &= \sum_{i=1}^N \log f(\mathbf{A}_i, \mathbf{x}_i, \boldsymbol{\theta}_i | \mathbf{d}_o, \boldsymbol{\vartheta}^{(h)}) + \log \phi(\boldsymbol{\theta}_i), \end{aligned} \quad (4)$$

where $\log f(\mathbf{A}_i, \mathbf{x}_i, \boldsymbol{\theta}_i | \mathbf{d}_o, \boldsymbol{\vartheta}^{(h)}) = \sum_{t=1}^{T_i} \log f(\mathbf{A}_{it} | \mathbf{x}_{it}, \boldsymbol{\theta}_i; \boldsymbol{\vartheta}^{(h)})$, $\mathbf{d}_o = \{(\mathbf{A}_i, \mathbf{x}_i)\}_{i=1}^N$ denotes the observed data, $\mathbf{d}_c = \{(\mathbf{A}_i, \mathbf{x}_i, \boldsymbol{\theta}_i)\}_{i=1}^N$ denotes the complete data, and $\boldsymbol{\vartheta}^{(h)}$ denotes the estimated value of $\boldsymbol{\vartheta}$ at the h -th iteration. Then, the expectation of the negative complete log-likelihood is

$$\begin{aligned} Q(\boldsymbol{\vartheta} | \boldsymbol{\vartheta}^{(h)}) &= \mathbb{E}[-\log(L_c(\mathbf{d}_c; \boldsymbol{\vartheta} | \mathbf{d}_o, \boldsymbol{\vartheta}^{(h)}))] \\ &= - \sum_{i=1}^N \int [\log f(\mathbf{A}_i | \mathbf{x}_i, \boldsymbol{\theta}_i; \boldsymbol{\vartheta}) + \log \phi(\boldsymbol{\theta}_i)] \phi(\boldsymbol{\theta}_i | \mathbf{d}_{i,o}; \boldsymbol{\vartheta}^{(h)}) d\boldsymbol{\theta}_i \\ &= - \sum_{i=1}^N \int \log f(\mathbf{A}_i | \mathbf{x}_i, \boldsymbol{\theta}_i; \boldsymbol{\vartheta}) \phi(\boldsymbol{\theta}_i | \mathbf{d}_{i,o}; \boldsymbol{\vartheta}^{(h)}) d\boldsymbol{\theta}_i - \sum_{i=1}^N \int \log \phi(\boldsymbol{\theta}_i) \phi(\boldsymbol{\theta}_i | \mathbf{d}_{i,o}; \boldsymbol{\vartheta}^{(h)}) d\boldsymbol{\theta}_i \\ &= Q_1(\boldsymbol{\vartheta} | \boldsymbol{\vartheta}^{(h)}) + Q_2(\boldsymbol{\vartheta}^{(h)}). \end{aligned} \quad (5)$$

To evaluate the integrals in Q_1 and Q_2 , we propose to approximate them with Metropolis-within-Gibbs (MwG) samples (Metropolis *and others*, 1953). To do this, we draw M independent MwG samples for each subject i . Specifically, let $\theta_{i,jj'}^{(h,m)}$ denote the m -th ($1 \leq m \leq M$) simulated sample of the (j, j') -th element of $\boldsymbol{\theta}_i$, given $\boldsymbol{\vartheta}^{(h)}$ and \mathbf{d}_o . We draw $\theta_{i,jj'}^{(h,m)}$ from $\mathcal{N}(\mu_{ijj'}^{(h)}, \sigma_{u,jj'}^2)$, where $\mu_{ijj'}^{(h)} = \mathbb{E}(\theta_{i,jj'} | \mathbf{d}_o; \boldsymbol{\vartheta}^{(h)})$ and $\sigma_{u,jj'}^2$ is the (j, j') -th element of $\boldsymbol{\Sigma}_u$. Here, $\boldsymbol{\Sigma}_u$ is a user-specified matrix, which can be obtained by fitting element-wise GLMMs to the data. In practice, we choose to use $M = 100$ to approximate the integrals.

Then, the Q-functions can be approximated by

$$\begin{aligned} Q_1(\boldsymbol{\vartheta}|\boldsymbol{\vartheta}^{(h)}) &= -\frac{1}{M} \sum_{m=1}^M \sum_{i=1}^N \log f(\mathbf{A}_i|\mathbf{x}_i, \boldsymbol{\theta}_i^{(h,m)}; \boldsymbol{\vartheta}), \\ Q_2(\boldsymbol{\vartheta}^{(h)}) &= -\frac{1}{M} \sum_{m=1}^M \sum_{i=1}^N \log \phi(\boldsymbol{\theta}_i^{(h,m)}). \end{aligned} \quad (6)$$

In the M-step, we aim to solve

$$\min_{\boldsymbol{\vartheta}} Q_1(\boldsymbol{\vartheta}|\boldsymbol{\vartheta}^{(h)}) + \gamma \|\mathbf{U}^\top \mathbf{U} - \mathbf{V}^\top \mathbf{V}\|_F^2, \text{ subject to } \|\mathbf{B}\|_0 \leq sn^2. \quad (7)$$

We propose to use the proximal gradient descent algorithm (Parikh and Boyd, 2014) to solve it. Let $F(\boldsymbol{\vartheta}) = Q_1(\boldsymbol{\vartheta}|\boldsymbol{\vartheta}^{(h)}) + \gamma \|\mathbf{U}^\top \mathbf{U} - \mathbf{V}^\top \mathbf{V}\|_F^2$. In the h_κ -th iteration for solving (7), we majorize $F(\boldsymbol{\vartheta})$ by a local quadratic function $\mathcal{Q}_c(\boldsymbol{\vartheta})$. That is,

$$F(\boldsymbol{\vartheta}) \leq \mathcal{Q}_c(\boldsymbol{\vartheta}) = F(\boldsymbol{\vartheta}^{(h_{\kappa-1})}) + [\nabla F(\boldsymbol{\vartheta}^{(h_{\kappa-1})})](\boldsymbol{\vartheta} - \boldsymbol{\vartheta}^{(h_{\kappa-1})}) + (c/2)(\boldsymbol{\vartheta} - \boldsymbol{\vartheta}^{(h_{\kappa-1})})^\top (\boldsymbol{\vartheta} - \boldsymbol{\vartheta}^{(h_{\kappa-1})}),$$

where c is a positive constant. Then, we solve $\min_{\boldsymbol{\vartheta}} \mathcal{Q}_c(\boldsymbol{\vartheta})$ subject to $\|\mathbf{B}\|_0 \leq sn^2$, which further transfers to the proximal problem of

$$\min_{\boldsymbol{\vartheta}} \frac{1}{2} \|\boldsymbol{\vartheta} - \{\boldsymbol{\vartheta}^{(h_{\kappa-1})} - c^{-1} \nabla F(\boldsymbol{\vartheta}^{(h_{\kappa-1})})\}\|_F^2, \text{ subject to } \|\mathbf{B}\|_0 \leq sn^2. \quad (8)$$

Its solution is given by $\boldsymbol{\vartheta}^{(h_\kappa)} = (\mathbf{U}^{(h_\kappa)}, \mathbf{V}^{(h_\kappa)}, \mathbf{B}^{(h_\kappa)})$, where

$$\begin{aligned} \mathbf{U}^{(h_\kappa)} &= \mathbf{U}^{(h_{\kappa-1})} - c^{-1} \nabla_{\mathbf{U}} F(\mathbf{U}^{(h_{\kappa-1})} \mathbf{V}^{(h_{\kappa-1})^\top}, \mathbf{B}^{(h_{\kappa-1})}), \\ \mathbf{V}^{(h_\kappa)} &= \mathbf{V}^{(h_{\kappa-1})} - c^{-1} \nabla_{\mathbf{V}} F(\mathbf{U}^{(h_\kappa)} \mathbf{V}^{(h_{\kappa-1})^\top}, \mathbf{B}^{(h_{\kappa-1})}), \\ \mathbf{B}^{(h_\kappa)} &= \text{Thr}(\mathbf{B}^{(h_{\kappa-1})} - c^{-1} \nabla_{\mathbf{B}} F(\mathbf{U}^{(h_\kappa)} \mathbf{V}^{(h_{\kappa-1})^\top}, \mathbf{B}^{(h_{\kappa-1})}), s), \end{aligned} \quad (9)$$

and $\text{Thr}(\mathbf{B}, s)$ is the hard-thresholding function defined as

$$[\text{Thr}(\mathbf{B}, s)]_{jj'l} = \begin{cases} \mathbf{B}_{jj'l} & \text{if } (j, j', l) \in \text{supp}(\mathbf{B}, s), \\ 0 & \text{otherwise,} \end{cases}$$

where $\text{supp}(\mathbf{B}, s)$ is the set of indices of \mathbf{B} corresponding to its largest sn^2 absolute values. This results in a sparse estimate of \mathbf{B} . We note that in (9), closed-form expressions for the gradients can be derived for specific GLMs. Furthermore, the learning rates in (9) are $1/c$ for \mathbf{U} , \mathbf{V} , and \mathbf{B} . In practice, different learning rates can be employed for these parameters to improve numerical performance. The M-step iterations can be terminated when

$$\max \left\{ \|\mathbf{U}^{(h_\kappa)} - \mathbf{U}^{(h_{\kappa-1})}\|_F^2, \|\mathbf{V}^{(h_\kappa)} - \mathbf{V}^{(h_{\kappa-1})}\|_F^2, \|\mathbf{B}^{(h_\kappa)} - \mathbf{B}^{(h_{\kappa-1})}\|_F^2 \right\} < \varepsilon_M,$$

where ε_M is a user-specified threshold. After the M-step is completed, the updated estimates of $\boldsymbol{\vartheta}$ can be used to re-draw MwG samples for the Q-functions in (6) and update the

E-step. Then, we iterate between the M- and E-steps until the objective function converges. The full details of the MCEM algorithm are in Algorithm 1.

For some applications, Θ is known to be a symmetric matrix. In that scenario, we factorize it as $\Theta = \mathbf{U}^\top \mathbf{\Lambda} \mathbf{U}$ where $\mathbf{\Lambda}$ is a $r \times r$ diagonal matrix with diagonal entries equal to -1 or 1. Letting $\vartheta = (\mathbf{U}, \mathbf{\Lambda}, \mathbf{B})$, we propose to solve

$$\min_{\vartheta} -l(\mathbf{U} \mathbf{\Lambda} \mathbf{U}^\top, \mathbf{B}) + \gamma \|\mathbf{U}^\top \mathbf{U} - \mathbf{U} \mathbf{\Lambda}^\top \mathbf{\Lambda} \mathbf{U}^\top\|_F^2, \text{ subject to } \|\mathbf{B}\|_0 \leq sn^2. \quad (10)$$

Similar as (9), Its solution at the h_κ -th iteration is given by $\vartheta^{(h_\kappa)} = (\mathbf{U}^{(h_\kappa)}, \mathbf{B}^{(h_\kappa)})$, where

$$\begin{aligned} \mathbf{U}^{(h_\kappa)} &= \mathbf{U}^{(h_{\kappa-1})} - c^{-1} \nabla_{\mathbf{U}} F(\mathbf{U}^{(h_{\kappa-1})} \mathbf{\Lambda} \mathbf{U}^{(h_{\kappa-1})^\top}, \mathbf{B}^{(h_{\kappa-1})}), \\ \mathbf{B}^{(h_\kappa)} &= \text{Thr}(\mathbf{B}^{(h_{\kappa-1})} - c^{-1} \nabla_{\mathbf{B}} F(\mathbf{U}^{(h_\kappa)} \mathbf{\Lambda} \mathbf{U}^{(h_\kappa)^\top}, \mathbf{B}^{(h_{\kappa-1})}), s). \end{aligned} \quad (11)$$

Accordingly, the M -step iterations can be terminated when

$$\max \left\{ \|\mathbf{U}^{(h_\kappa)} - \mathbf{U}^{(h_{\kappa-1})}\|_F^2, \|\mathbf{B}^{(h_\kappa)} - \mathbf{B}^{(h_{\kappa-1})}\|_F^2 \right\} < \varepsilon_M.$$

The details of this alternative MCEM algorithm is described in Algorithm 2.

3.1 Tuning Parameter Selections

Our algorithm contains two tuning parameters r and s that require tuning to achieve good numerical performance. We propose a computationally efficient two-stage approach to select the optimal tuning parameters. In the first stage, we fix $s = 0$ and choose the optimal integer of r that minimizes the Extended Bayesian Information Criterion (EBIC)(Chen and Chen, 2008), defined as

$$EBIC = -2\ell(\hat{\vartheta}) + [\log(n^2 N) + C \log\{n^2(p+1)\}] \times (2nr + spn^2), \quad (12)$$

where $\ell(\hat{\vartheta})$ is as defined in (2) and C is a user-specified constant that is set to 1/2 by us. In the second stage, we fix r at the optimal value chosen in the first stage and perform a grid search of s that minimizes the EBIC defined in (12). That results in the optimal combination of r and s being used in our proposed method.

4 Simulation

We conduct simulation studies to compare the numerical performance of our proposed method, named as MR-GLMM, with two element-wise penalized generalized linear mixed models. In these two models, each entry of the response matrix is regressed on the covariates by a generalized linear mixed model. More specifically, suppose $A_{it,jj'}$ is the (j, j') -th entry of \mathbf{A}_{it} . These element-wise models assume that

$$g(A_{it,jj'}) = \Theta_{jj'} + \theta_{i,jj'} + \sum_{l=1}^p x_{iil} \mathbf{B}_{jj'l},$$

Algorithm 1: Monte Carlo Expectation Maximization Algorithm (MCEM)

Input: Matrix response \mathbf{A} and covariate tensor \mathbf{X} .

Output: $\tilde{\mathbf{U}}$, $\tilde{\mathbf{V}}$, and $\tilde{\mathbf{B}}$ as solutions to (3).

Initialization:

Compute $\bar{\mathbf{A}} = \frac{1}{N} \sum_{i=1}^N \mathbf{A}_i$ and let $SVD_r(g(\bar{\mathbf{A}})) = [\bar{\mathbf{U}}_0, \bar{\Sigma}_0, \bar{\mathbf{V}}_0]$. Set $\mathbf{U}^{(0)} = \bar{\mathbf{U}}_0 \bar{\Sigma}_0^{1/2}$ and $\mathbf{B}^{(0)} = \mathbf{0}$.

Repeat

At the h -th iteration, do

E-step:

Select the initial value $\boldsymbol{\theta}_i^{(h,0)} \sim \mathcal{N}_d(\mathbf{0}, \mathbf{I}_d)$,

For $m = 1, \dots, M$, perform Metropolis-within-Gibbs sampling as follows:

Sub-step 1: Let $\boldsymbol{\theta}_i^\dagger = \boldsymbol{\theta}_i^{(h,m-1)} + \boldsymbol{\xi}$, where $\boldsymbol{\xi}$ is an $n \times n$ matrix with each entry from $N(0, \sigma_\theta^2)$, and σ_θ^2

is a user-specified value.

Sub-step 2: With f being defined as in (6), let

$$\boldsymbol{\theta}_i^{(h,m)} = \begin{cases} \boldsymbol{\theta}_i^\dagger, & \text{with probability } \min \left\{ 1, \frac{f(\boldsymbol{\theta}_i^\dagger)}{f(\boldsymbol{\theta}_i^{(h,m-1)})} \right\}, \\ \boldsymbol{\theta}_i^{(h,m-1)}, & \text{otherwise.} \end{cases}$$

Update Q_1 and Q_2 in (6) with $\{\boldsymbol{\theta}_i^{(h,m)}\}_{m=1}^M$.

M-step:

Initialize: Set $c = c^{(0)}$, a user-specified value.

Repeat: At the h_κ -th iteration for $\kappa \geq 1$,

Sub-step 1: Let $\boldsymbol{\vartheta}^{(h_\kappa)}$ be defined as in (9) with $c = c^{(h_{\kappa-1})}$;

Sub-step 2: Break if $F(\boldsymbol{\vartheta}^{(h_\kappa)}) \leq \mathcal{Q}_c(\boldsymbol{\vartheta}^{(h_{\kappa-1})})$;

Sub-step 3: Otherwise, let $c = 2c$ and return to Sub-step 1.

Until

$$\max \left\{ \|\mathbf{U}^{(h_\kappa)} - \mathbf{U}^{(h_{\kappa-1})}\|_F^2, \|\mathbf{V}^{(h_\kappa)} - \mathbf{V}^{(h_{\kappa-1})}\|_F^2, \|\mathbf{B}^{(h_\kappa)} - \mathbf{B}^{(h_{\kappa-1})}\|_F^2 \right\} < \varepsilon_M.$$

Until the objective function converges and set $\tilde{\mathbf{U}}$, $\tilde{\mathbf{V}}$, and $\tilde{\mathbf{B}}$ as the terminating values.

Algorithm 2: Monte Carlo Expectation Maximization Algorithm with Symmetrization

Input: Matrix response \mathbf{A} , covariate tensor \mathbf{X} and $\tilde{\mathbf{U}}, \tilde{\mathbf{V}}$, and $\tilde{\mathbf{B}}$ from Algorithm 1.
Output: $\hat{\mathbf{U}}, \hat{\mathbf{\Lambda}}$ and $\hat{\mathbf{B}}$ as solutions to (10).

Initialization:

Let $\hat{\mathbf{\Lambda}}$ be a diagonal matrix with the i -th diagonal entry $\hat{\Lambda}_{ii} = \text{sign}(\tilde{\mathbf{U}}_{.i}^\top \tilde{\mathbf{V}}_{.i})$,
 $\mathbf{U}^{(0)} = \frac{\tilde{\mathbf{U}} + \hat{\mathbf{\Lambda}} \tilde{\mathbf{V}}^\top}{2}$ and $\mathbf{B}^{(0)} = \tilde{\mathbf{B}}$.

Repeat

At the h -th iteration, do

E-step:

Select the initial value $\boldsymbol{\theta}_i^{(h,0)} \sim \mathcal{N}_d(\mathbf{0}, \mathbf{I}_d)$,

For $m = 1, \dots, M$, perform Metropolis-within-Gibbs sampling as follows:

Sub-step 1: Let $\boldsymbol{\theta}_i^\dagger = \boldsymbol{\theta}_i^{(h,m-1)} + \boldsymbol{\xi}$, where $\boldsymbol{\xi}$ is an $n \times n$ matrix with each entry from $N(0, \sigma_\theta^2)$, and σ_θ^2

is a user-specified value.

Sub-step 2: With f defined as in (6), let

$$\boldsymbol{\theta}_i^{(h,m)} = \begin{cases} \boldsymbol{\theta}_i^\dagger, & \text{with probability } \min \left\{ 1, \frac{f(\boldsymbol{\theta}_i^\dagger)}{f(\boldsymbol{\theta}_i^{(h,m-1)})} \right\}, \\ \boldsymbol{\theta}_i^{(h,m-1)}, & \text{otherwise.} \end{cases}$$

Update Q_1 and Q_2 in (6) with $\{\boldsymbol{\theta}_i^{(h,m)}\}_{m=1}^M$.

M-step:

Initialize: Set $c = c^{(0)}$, a user-specified value.

Repeat: at the h_κ -th iteration for $\kappa \geq 1$

Sub-step 1: Let $\boldsymbol{\vartheta}^{(h_\kappa)}$ be as defined in (11) with $c = c^{(h_{\kappa-1})}$;

Sub-step 2: Break if $F(\boldsymbol{\vartheta}^{(h_\kappa)}) \leq \mathcal{Q}_c(\boldsymbol{\vartheta}^{(h_{\kappa-1})})$;

Sub-step 3: Otherwise, let $c = 2c$ and return to Sub-step 1.

Until

$$\max \left\{ \|\mathbf{U}^{(h_\kappa)} - \mathbf{U}^{(h_{\kappa-1})}\|_F^2, \|\mathbf{B}^{(h_\kappa)} - \mathbf{B}^{(h_{\kappa-1})}\|_F^2 \right\} < \varepsilon_M.$$

Until the objective function converges and set $\hat{\mathbf{U}}$ and $\hat{\mathbf{B}}$ as the terminating values.

where $g(\cdot)$ is the link function, $\Theta_{jj'}$, $\theta_{i,jj'}$ and $\mathcal{B}_{jj'l}$ are the (j, j') -th entry of Θ , θ_i and $\mathcal{B}_{:,:,l}$ respectively. In other words, the element-wise model can be treated as a special case of our proposed model in (1) without considering the matrix structure. To obtain sparse estimates of \mathcal{B} , we solve the following penalized GLMM optimization problem for each (j, j') with $1 \leq j, j' \leq n$:

$$\min_{\boldsymbol{\vartheta}_{jj'}} -l(\boldsymbol{\vartheta}_{jj'}) + \nu_{jj'} \sum_{l=1}^p p(\mathcal{B}_{jj'l}),$$

where $\boldsymbol{\vartheta}_{jj'} = (\Theta_{jj'}, \mathcal{B}_{jj'1}, \dots, \mathcal{B}_{jj'p})^\top$ is the vector of parameters, $l(\boldsymbol{\vartheta}_{jj'})$ is the element-wise observed log-likelihood function similarly as defined in (2), and $p(\cdot)$ is a penalty function with tuning parameter $\nu_{jj'}$. We choose L_1 and SCAD penalties and call these two element-wise models as GLMM-LASSO and GLMM-SCAD respectively. In our numerical studies, we implement these element-wise models by using the **rpql** R package (Hui *and others*, 2017). The optimal tuning parameters in these models are chosen by cross-validation.

To compare the three methods, we evaluate their performance using three metrics. For Θ , we calculate the Frobenius norm error $\|\widehat{\Theta} - \Theta\|_F$. For \mathcal{B} , we calculate both the Frobenius norm error $\|\widehat{\mathcal{B}} - \mathcal{B}\|_F$ and the sensitivity and specificity of $\widehat{\mathcal{B}}$ given by the three methods. The sensitivity is defined as the proportion of true nonzero entries of \mathcal{B} that are correctly estimated as nonzero, and the specificity is defined as the proportion of true zero entries of \mathcal{B} that are correctly estimated as zero. We consider the following two models

$$\text{Model 1 (Linear regression): } \mathbf{A}_{it} = \Theta + \theta_i + \sum_{l=1}^p x_{itl} \mathcal{B}_{:,:,l} + \epsilon_{it},$$

$$\text{Model 2 (Logistic regression): } \text{logit}(P(\mathbf{A}_{it} = 1)) = \Theta + \theta_i + \sum_{l=1}^p x_{itl} \mathcal{B}_{:,:,l}.$$

We generate covariates x_{itl} ($1 \leq i \leq N$, $1 \leq t \leq T_i$ and $1 \leq l \leq p$) independently from $\mathcal{N}(0, 1)$ and Θ as $\Theta = \mathbf{U}\mathbf{U}^\top$, where each entry of $\mathbf{U} \in \mathbb{R}^{n \times r}$ is generated from $\mathcal{N}(0, 1)$. We independently generate each entry of θ_i ($1 \leq i \leq N$) from $\mathcal{N}(0, 4)$. For each entry of \mathcal{B} , we generate it from Bernoulli(2, s), where $s = 0.1$ or 0.2 , which renders a sparse tensor of \mathcal{B} with approximately 10% and 20% nonzero entries equal to 2. Moreover, in Model 1, we generate each entry of ϵ_{it} from $\mathcal{N}(0, 0.25)$. In all simulations, we set $n = 30$, $p = 5$, $T_i = 5$ for all $1 \leq i \leq N$ and choose $r = 2$ or 3 . For all scenarios, we run 100 simulations to calculate the means and standard deviations of the aforementioned three metrics.

The simulation results are tabulated in Tables 1 and 2. The results demonstrate that our proposed method substantially outperforms the two alternative methods across all scenarios and metrics. For the estimation error of Θ , our method consistently achieves much smaller errors in all cases. This superior performance arises from our method's modeling of the low-rank structure of Θ , which the two element-wise GLMM models fail to utilize. Regarding variable selection and estimation error of \mathcal{B} , our method achieves nearly perfect selection performance, exhibiting high sensitivity and specificity across all cases. In contrast, despite employing penalization techniques to produce sparse estimators of \mathcal{B} , the GLMM-LASSO and GLMM-SCAD methods exhibit inferior variable selection performance compared to our approach, particularly in terms of sensitivity. This deficiency again arises from their

(n, p)	N	r	s	Method	$\ \widehat{\Theta} - \Theta\ _F$	$\ \widehat{\mathcal{B}} - \mathcal{B}\ _F$	Sensitivity	Specificity
(30, 5)	200	2	0.1	MR-GLMM	0.59(0.09)	5.84(2.34)	0.99(0.01)	1.00(0.00)
				GLMM-LASSO	2.94(0.83)	37.78(0.16)	0.22(0.01)	0.30(0.01)
				GLMM-SCAD	2.91(0.81)	37.11(0.25)	0.24(0.01)	0.29(0.01)
			0.2	MR-GLMM	0.70(0.08)	6.63(3.01)	1.00(0.00)	1.00(0.00)
				GLMM-LASSO	4.17(1.21)	53.34(0.19)	0.25(0.01)	0.53(0.01)
				GLMM-SCAD	3.91(1.04)	48.13(0.45)	0.36(0.01)	0.45(0.01)
		3	0.1	MR-GLMM	1.22(0.29)	9.08(2.57)	0.97(0.02)	1.00(0.00)
				GLMM-LASSO	3.33(0.59)	37.97(0.09)	0.23(0.01)	0.34(0.01)
				GLMM-SCAD	3.20(0.54)	35.46(0.38)	0.31(0.02)	0.30(0.01)
			0.2	MR-GLMM	1.22(0.22)	9.48(3.17)	0.99(0.01)	1.00(0.00)
				GLMM-LASSO	4.44(1.27)	53.30(0.17)	0.25(0.01)	0.53(0.01)
				GLMM-SCAD	4.14(1.12)	48.15(0.38)	0.36(0.01)	0.46(0.01)
	400	2	0.1	MR-GLMM	0.94(0.12)	3.48(1.81)	0.99(0.01)	1.00(0.00)
				GLMM-LASSO	2.47(0.59)	37.80(0.13)	0.22(0.01)	0.30(0.01)
				GLMM-SCAD	2.45(0.58)	37.38(0.21)	0.23(0.01)	0.29(0.01)
			0.2	MR-GLMM	0.83(0.15)	4.01(1.77)	0.98(0.01)	1.00(0.00)
				GLMM-LASSO	3.34(0.68)	53.36(0.16)	0.25(0.01)	0.51(0.01)
				GLMM-SCAD	3.18(0.60)	48.43(0.37)	0.35(0.01)	0.44(0.01)
		3	0.1	MR-GLMM	0.86(0.17)	6.57(2.70)	0.99(0.01)	1.00(0.00)
				GLMM-LASSO	2.82(0.38)	37.77(0.11)	0.24(0.01)	0.29(0.01)
				GLMM-SCAD	2.75(0.34)	35.63(0.31)	0.30(0.01)	0.27(0.01)
			0.2	MR-GLMM	1.48(0.38)	6.02(2.50)	0.96(0.02)	1.00(0.00)
				GLMM-LASSO	3.35(0.73)	53.31(0.18)	0.25(0.01)	0.51(0.01)
				GLMM-SCAD	3.15(0.63)	48.21(0.41)	0.36(0.01)	0.44(0.01)

Table 1: Simulation results for Model 1.

failure to leverage the matrix structure of \mathcal{B} . Additionally, we observe that the estimation errors of \mathcal{B} obtained by our method are substantially smaller than those produced by the two alternatives. In summary, the simulation studies provide compelling evidence that our method possesses significant advantages over element-wise approaches.

5 Applications to brain imaging data

5.1 DTI imaging data

We apply our method to analyze an ADNI brain imaging dataset acquired using DTI. The cohort consists of $N = 250$ healthy control participants, aged 55 to 89 years, who are at risk for Alzheimer’s disease. For each subject, DTI scans produce 100 measurements corresponding to tractography-based brain connectivity measures derived from non-overlapping segments along white matter fiber tracts. These 100 repeated measures are grouped into 5 consecutive time windows, each comprising 20 measurements. Within each window, we use these 20 samples to compute the sample covariance matrix among 90 ROIs, denoted as $A_{it} \in \mathbb{R}^{90 \times 90}$, which represents the structural brain network of subject i at time window

(n, p)	N	r	s	Method	$\ \widehat{\Theta} - \Theta\ _F$	$\ \widehat{\mathcal{B}} - \mathcal{B}\ _F$	Sensitivity	Specificity		
(30, 5)	200	2	0.1	MR-GLMM	2.27(3.1)	4.12(2.22)	0.99(0.01)	1(0)		
				GLMM-LASSO	12.92(1.82)	42.28(0.01)	0.51(0.04)	1(0)		
				GLMM-SCAD	12.94(1.78)	42.29(0.01)	0.56(0.04)	1(0)		
				0.2		MR-GLMM	3.35(4.33)	5.64(2.86)	0.99(0.01)	1(0)
						GLMM-LASSO	17.79(3.57)	59.85(0.01)	0.39(0.03)	1(0)
						GLMM-SCAD	17.79(3.57)	59.84(0.01)	0.47(0.05)	1(0)
				3	0.1	MR-GLMM	2.33(2.02)	9.18(3.25)	0.99(0.01)	1(0)
						GLMM-LASSO	15.84(1.71)	42.3(0.02)	0.45(0.05)	1(0)
						GLMM-SCAD	15.84(1.71)	42.3(0.01)	0.52(0.04)	1(0)
		0.2		MR-GLMM	2.64(2.07)	11.23(3.61)	0.99(0.01)	1(0)		
				GLMM-LASSO	21.63(2.38)	59.85(0.01)	0.37(0.04)	1(0)		
				GLMM-SCAD	21.63(2.38)	59.85(0.01)	0.43(0.02)	1(0)		
	400	2	0.1	MR-GLMM	2.03(2.38)	3.47(2.36)	0.99(0.02)	1(0)		
				GLMM-LASSO	13.58(2.02)	42.28(0.01)	0.59(0.03)	1(0)		
				GLMM-SCAD	13.58(2.02)	42.28(0.01)	0.62(0.03)	1(0)		
				0.2		MR-GLMM	3.32(4.41)	4.73(2.81)	0.99(0.01)	1(0)
						GLMM-LASSO	17.32(2.41)	59.82(0.01)	0.52(0.04)	1(0)
						GLMM-SCAD	17.32(2.41)	59.82(0.01)	0.57(0.03)	1(0)
				3	0.1	MR-GLMM	3.52(4.03)	5.4(2.33)	0.99(0.01)	1(0)
						GLMM-LASSO	15.45(2.01)	42.28(0.01)	0.58(0.04)	1(0)
						GLMM-SCAD	15.46(2.04)	42.28(0.01)	0.62(0.03)	1(0)
		0.2		MR-GLMM	5.09(3.2)	6.59(3.49)	0.97(0.02)	1(0)		
				GLMM-LASSO	21.86(2.52)	59.84(0.01)	0.48(0.04)	1(0)		
				GLMM-SCAD	21.98(2.74)	59.85(0.04)	0.54(0.03)	1(0)		

Table 2: Simulation results for Model 2.

$t \in \{1, \dots, 5\}$. We hypothesize that (1) AD risk factors such as age and APOE4 carrier status may induce alterations in the brain connectome, and (2) these detrimental effects exhibit sexual differences.

To verify our hypothesis, we regress A_{it} on age, sex, APOE4 and DX status by our proposed matrix-response linear models:

$$\text{Model 1 : } \mathbf{A}_{it} = \Theta + \theta_i + \mathcal{B}_1 \text{Sex}_i + \mathcal{B}_2 \text{Age}_i + \mathcal{B}_3 \text{Sex}_i \times \text{Age}_i + \epsilon_{it}.$$

$$\text{Model 2 : } \mathbf{A}_{it} = \Theta + \theta_i + \mathcal{B}_1 \text{Sex}_i + \mathcal{B}_2 \text{APOE4}_i + \mathcal{B}_3 \text{Sex}_i \times \text{APOE4}_i + \epsilon_{it}.$$

$$\text{Model 3 : } \mathbf{A}_{it} = \Theta + \theta_i + \mathcal{B}_1 \text{Sex}_i + \mathcal{B}_2 \text{DX}_i + \mathcal{B}_3 \text{Sex}_i \times \text{DX}_i + \epsilon_{it}.$$

In these models, female serves as the reference category for sex. APOE4 status is treated as an ordinal variable with three levels: no copies (non-carriers), one copy (heterozygous carriers), and two copies (homozygous carriers) of the APOE4 allele. Diagnostic (DX) status is also treated as an ordinal variable representing AD progression, ranging from Cognitively Normal (CN), Subjective Memory Complaints (SMC), Early/Late Mild Cognitive Impairment (EMCI/LMCI), to Alzheimer's Disease (AD).

For each model, we initialize our algorithm by running an elementwise linear mixed model and using the resulting estimators as the initial estimators of $\mathcal{B}_1, \mathcal{B}_2$ and \mathcal{B}_3 . The

optimal values of tuning parameters are selected by the EBIC within the range that $r \in \{1, 2, 3, 4\}$ and $s \in \{0.01, 0.02, 0.05, 0.08, 0.1\}$. To visualize $\hat{\Theta}$ obtained by our method, we present heatmaps of $\hat{\Theta}$ for each model and apply K -means clustering to the rows and columns of $\hat{\Theta}$. The optimal number of clusters is determined using the Silhouette method (Rousseeuw, 1987), which evaluates clustering quality by measuring how similar objects are to their assigned cluster compared to other clusters, through a combination of intra-cluster cohesion and inter-cluster separation metrics. We then identify regions from the heatmaps that correspond to the eight established brain functional modules: Visual, Sensorimotor, Dorsal Attention, Ventral Attention, Limbic, Frontoparietal, Default Mode, and Cerebellum modules. These modules represent distinct neural networks associated with various cognitive and sensory functions, providing a structured framework for interpreting the patterns observed in our analysis. To visualize $\hat{\mathcal{B}}_j$ obtained by our method, we plot the axial and sagittal views of the networks identified by $\hat{\mathcal{B}}_j$. Specifically, for each nonzero entry in $\hat{\mathcal{B}}_j$, we draw an edge between the two ROIs corresponding to that entry. To simplify the presentation of these networks, all ROIs are grouped into the eight functional modules.

The results for Model 1 are shown in Figures 1 and 2. In Figure 1, Module 1 exhibits positive correlations among the Default Mode network (DMN), Visual network (VN), Frontoparietal network (FPN), Sensorimotor network (SMN), and Ventral Attention network (VAN), suggesting coordinated activity in cognitive, sensory, and attentional processing. Module 2 demonstrates connectivity patterns linking the DMN, Limbic network (LN), and VN, and SMN, elucidating the integration between higher-order cognitive functions and affective processing systems. Module 3 expands this pattern, incorporating the Dorsal Attention network (DAN), which indicates a broader integration of attentional control. Notably, DMN and VN remain consistently correlated across all groups, highlighting their fundamental role in intrinsic brain connectivity. Figure 2(a) shows that with increasing age, the VN, LN, FPN, and DMN exhibit stronger positive inter-correlations, suggesting enhanced connections among these large-scale cognitive and associative networks with aging. On the other hand, the connections between LN, SMN, and DMN are reduced, indicating a potential shift in emotional regulation and sensorimotor processing with aging. The age and sex interactions depicted in Figure 2(b) reveals that older males demonstrate reduced inter-module correlations across all major networks—with the exception of the Cerebellum—when compared to younger females. This pattern suggests that large-scale brain network connectivity undergoes age- and sex-dependent modulation, potentially reflecting differences in neuroplasticity and the adaptation of functional interactions throughout the lifespan.

The results for Model 2 are shown in Figures 3 and 4. In Figure 3, Module 1 exhibits extensive connectivity across multiple networks—DMN, LN, VN, FPN, SMN, and DAN—suggesting robust integration between cognitive, emotional, and attentional systems. Module 2 displays a similar connectivity profile but excludes the DAN, indicating a more focused functional integration primarily involving cognitive processes, sensory integration, and emotional regulation. Module 3 shows a more selective connectivity pattern, connecting only the DMN, VN, SMN, and VAN, potentially reflecting a greater emphasis on externally-oriented attentional processing. Notably, despite these regional differences, the DMN, VN, and SMN maintain positive correlations across all regions, underscoring their

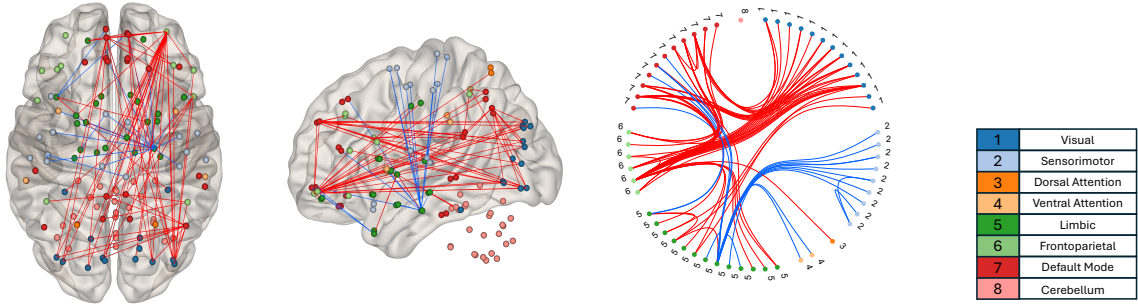


Module	Large-scale functional networks
1	Default Mode, Visual, Frontoparietal, Sensorimotor, Ventral Attention
2	Default Mode, Limbic, Visual, Sensorimotor
3	Default Mode, Limbic, Visual, Sensorimotor, Dorsal Attention

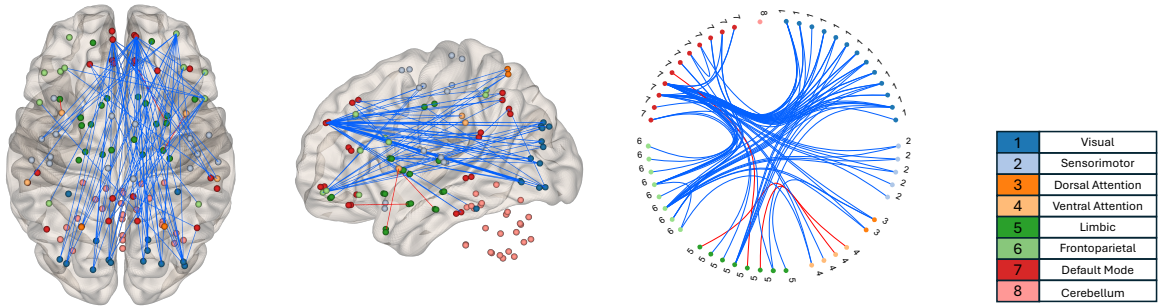
Figure 1: The heatmap of $\hat{\Theta}$ in Model 1, where rows and columns are arranged according to the K -means clustering. The black dashed lines represent the groups of functional modules identified in the clustering process with module names on the right table.

fundamental importance in the brain’s intrinsic functional architecture. Figure 4(a) reveals that APOE4 carriers exhibit progressively stronger negative inter-correlations between LN and VN, SMN, FPN, and DMN. Additionally, both DN and VAN in APOE4 carriers display negative associations with the Limbic system, suggesting widespread disruption in functional integration across multiple cognitive and sensorimotor domains. We also observe negative correlations between SMN and both LN and DMN, potentially reflecting APOE4-associated disruptions in the coordination of motor functions, emotional processing, and internally directed cognitive processes. Regarding sex and APOE4 interactions shown in Figure 4, male participants with elevated APOE4 levels demonstrate stronger inter-module connectivity across all major networks except the Cerebellum, compared to both males with lower APOE4 levels and females regardless of APOE4 status. This pattern suggests sex-specific modulation of large-scale brain network organization, possibly reflecting compensatory neural mechanisms or differential vulnerability to APOE4-associated neurobiological changes.

The results for Model 3 are illustrated in Figures 5 and 6. Figure 5 shows that Module 1 is contained in DMN, which is known to mediate self-referential thought and introspection. Module 3 is completely encompassed by the VN, representing areas involved in primary and secondary visual processing. Likewise, Module 4 is entirely contained within LN, which is crucial for emotion regulation and memory formation. In contrast, Modules 2 and 5 comprise nodes from multiple large-scale networks—FPN, SMN, VAN, and DMN—suggesting their involvement in complex cognitive functions, attentional processes, and motor coordination. Figure 6(a) illustrates that Alzheimer’s disease progression, characterized by symptoms of memory impairment and cognitive decline, is associated with progressively stronger negative inter-correlations between LN and several other networks, including VN, SMN, FPN, and DMN. Additionally, specific regions within both DN and VAN show negative associations with the Limbic system. These patterns suggest widespread disruption in



(a) Axial and sagittal views of $\widehat{\mathcal{B}}_2$ and the corresponding functional region network.



(b) Axial and sagittal views of $\widehat{\mathcal{B}}_3$ and the corresponding functional region network.

Figure 2: Estimated $\widehat{\mathcal{B}}_2$ and $\widehat{\mathcal{B}}_3$ in Model 1. Red and blue edges indicate positive and negative entries in $\widehat{\mathcal{B}}_2$ and $\widehat{\mathcal{B}}_3$, respectively.

functional integration across multiple cognitive and sensorimotor domains as AD severity increases. Conversely, Figure 6(b) shows that males with escalated AD progression exhibit stronger inter-module connectivity throughout nearly all major networks, with the exception of the Cerebellum. This enhanced connectivity in males with elevated AD progression is evident when compared both to males at early stage and to females across all AD stages.

These findings align with established sex-specific differences in large-scale brain networks. Previous research has documented that males typically exhibit stronger right-lateralized connectivity patterns (Tomasi and Volkow, 2012), while females demonstrate greater interhemispheric integration, potentially contributing to distinct compensatory mechanisms during neurodegenerative progression. Furthermore, neurodegenerative diseases characteristically target specific functional modules rather than causing uniform atrophy, which prompts compensatory reorganization within brain networks (Ingalhalikar and others, 2014). The observed increase in inter-module connectivity among males with elevated disease status likely represents an adaptive response aimed at preserving functional stability despite ongoing network disruptions.

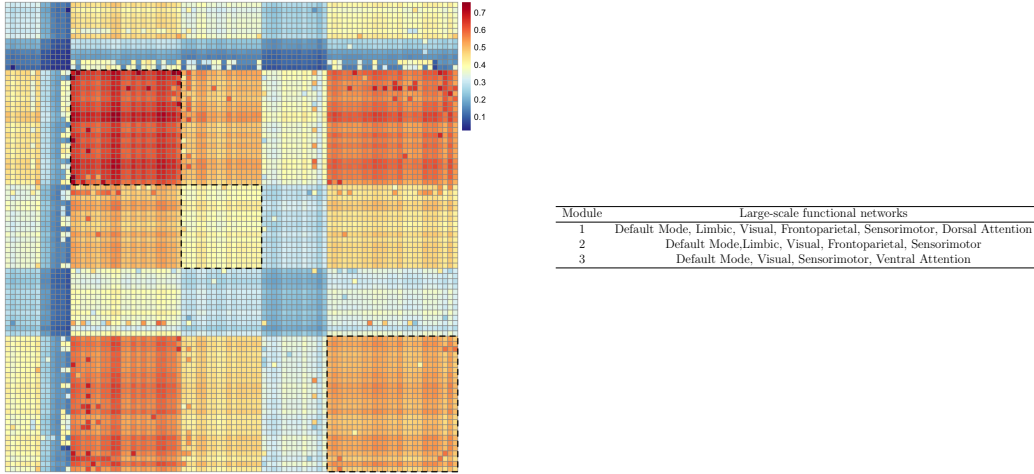


Figure 3: The heatmap of $\hat{\Theta}$ in Model 2, where rows and columns are arranged according to the K -means clustering. The black dashed lines represent the groups of functional modules identified in the clustering process with module names on the right table.

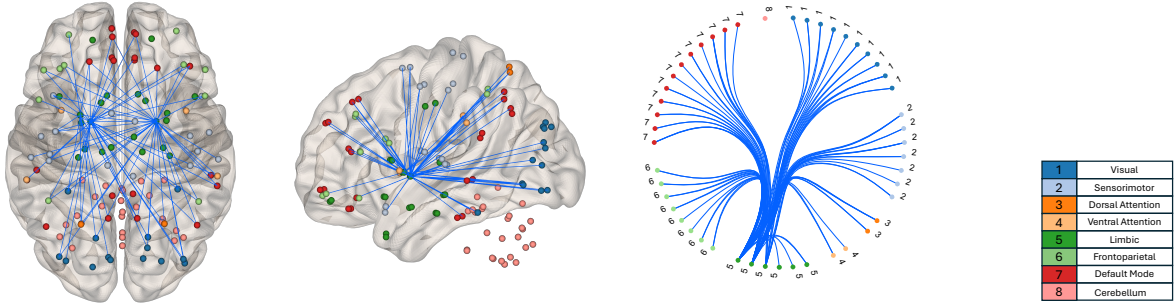
5.2 Functional MRI Data

There is growing evidence that functional connectivity in the resting state exhibits remarkable self-organized fluctuations, which is relevant to understanding dementia progression (Smith *and others*, 2013). To investigate this phenomenon, we analyze functional MRI (fMRI) data from the Human Connectome Project (Van Essen *and others*, 2013), comprising 260 subjects who underwent both resting-state and task-based imaging sessions. During scanning, each subject completed five sequential stages, alternating between resting states and tongue-movement tasks. We extract blood-oxygen-level-dependent (BOLD) time series from 50 regions of interest (ROIs) across 30 time points. These time points are divided into five consecutive, non-overlapping time windows ($T = 5$), with the first and last windows corresponding to resting-state periods and the three middle windows to tongue-movement tasks. Within each time window, we use 6 time points to compute the sample covariance matrix of BOLD signals across the 50 ROIs. This results in a 50×50 covariance matrix A_{it} representing the functional connectivity network for subject i at time window t . We then fit the following matrix-response model:

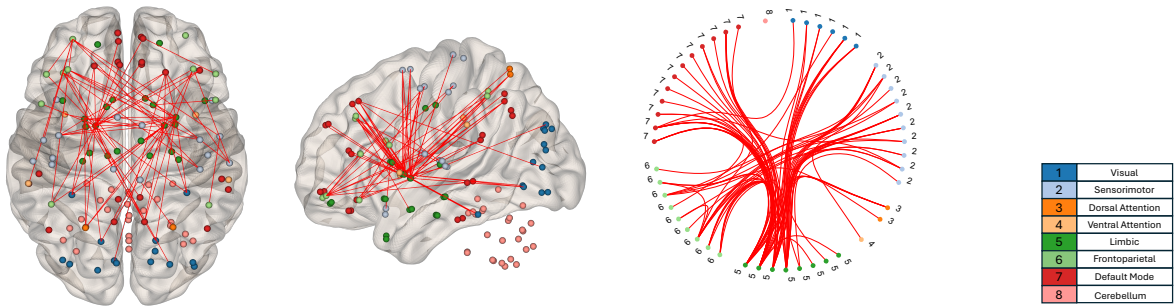
$$A_{it} = \Theta + \theta_i + \mathcal{B}_1 \text{Status}_{it} + \epsilon_{it}, \quad (13)$$

where Θ is the fixed intercept term, θ_i is the random intercept, Status_{it} is the stage indicator variable ($\text{Status}_{it} = 1$ for the action stage and $\text{Status}_{it} = 0$ for the resting stage), and ϵ_{it} is the error term. In our algorithm, the optimal values of tuning parameters r and s are selected using the eBIC criterion. We visualize the resulting $\hat{\Theta}$ and $\hat{\mathcal{B}}_1$ in the same manner as described in Section 5.1, with the results displayed in Figures 7 and 8, respectively.

In Figure 7, the positive entries in Module 1 correspond to various visual modules, highlighting the significance of visual processing when subjects respond to visual cues for status changes. Module 2 encompasses the posterior cingulate cortex, a central hub in DMN. The positive values in this region underscore its critical function in sustaining



(a) Axial and sagittal views of $\widehat{\mathcal{B}}_2$ and the corresponding functional region network.



(b) Axial and sagittal views of $\widehat{\mathcal{B}}_3$ and the corresponding functional region network.

Figure 4: Estimated $\widehat{\mathcal{B}}_2$ and $\widehat{\mathcal{B}}_3$ in Model 2. Red and blue edges indicate positive and negative entries in $\widehat{\mathcal{B}}_2$ and $\widehat{\mathcal{B}}_3$, respectively.

elevated metabolic activity during resting states. Module 3, which incorporates the dorsal stream and superior parietal cortex, displays positive entries that support these areas’ continuous engagement in spatial information processing, even when no specific task is required. Module 4 relates to somatosensory and motor-related brain regions, with positive values indicating maintained levels of motor readiness and sensory processing—reflecting the intrinsic functional state necessary for swift motor execution.

The results of $\widehat{\mathcal{B}}_1$ presented in Figure 8 demonstrate a positive influence of tongue stimulation on the covariance between identified cortical regions. Positive entries corresponding to MT+ Complex and Neighboring Visual Areas, Dorsal Stream Visual, Early Visual, and Ventral Stream Visual indicate that the intrinsic connectivity within the visual processing network is preserved, potentially reflecting cross-modal interactions induced by tongue stimulation that operate alongside baseline visual system dynamics. Similarly, positive entries among somatosensory and motor regions, including Somatosensory and Motor and Premotor nodes, emphasize the sensorimotor system’s capacity to maintain functional integration even when processing localized somatosensory input from the tongue. Furthermore, enhanced correlations among Posterior Cingulate (PC) nodes, a key component of DMN, suggest that intrinsic connectivity in this region remains intact despite external sensory stimulation. This observation is consistent with the PC’s established role in integrating internal and external information. These findings lead us to conclude that tongue stimulation

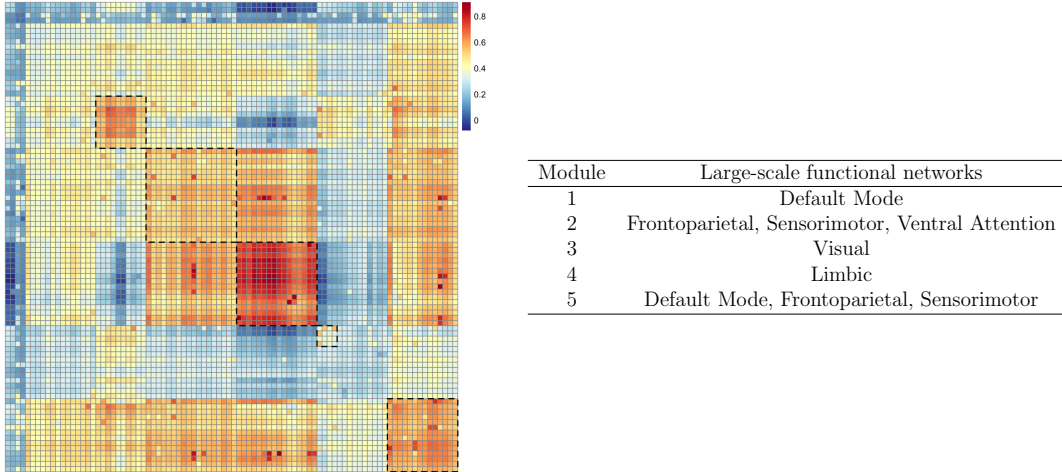
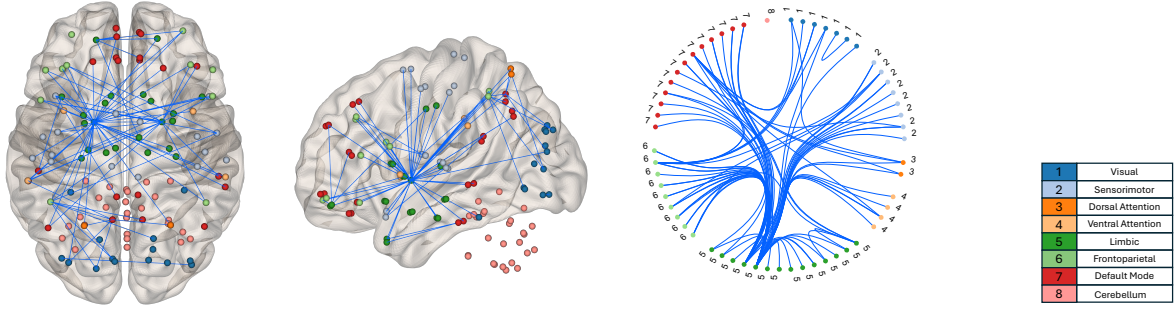


Figure 5: The heatmap of $\hat{\Theta}$ in Model 3, where rows and columns are arranged according to the K -means clustering. The black dashed lines represent the groups of functional modules identified in the clustering process with module names on the right table.

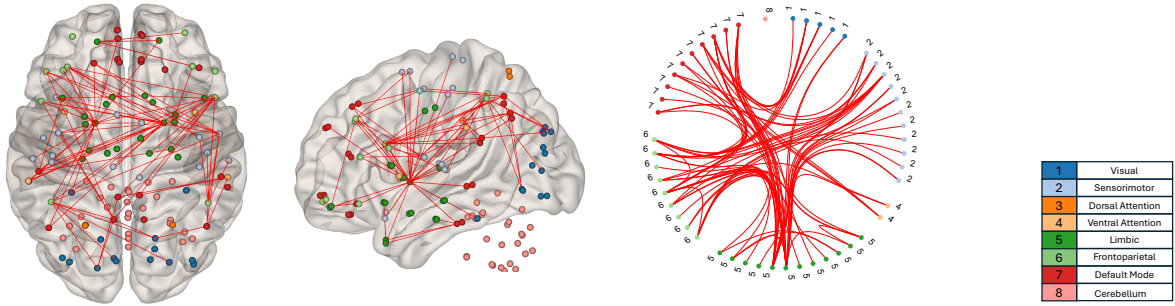
increases covariance between signals in the relevant ROIs, aligning with recent research on the effects of motor stimulation on brain connectivity.

6 Discussion

In this article, we have introduced a novel class of matrix-response generalized linear mixed models (MR-GLMMs) specifically designed for analyzing longitudinal brain imaging data. Our approach addresses a critical gap in the neuroimaging literature by providing a unified framework that can handle matrix-valued responses while accounting for both between-subject heterogeneity through random effects and within-subject temporal correlations inherent in longitudinal designs. The proposed MR-GLMM method extends traditional generalized linear mixed models to accommodate matrix-valued responses through several key innovations. First, we model the conditional mean of the matrix response using a linear combination of time-varying covariates with matrix-valued coefficients, incorporating both fixed population-level effects and subject-specific random effects. To ensure computational tractability and statistical interpretability, we impose a low-rank constraint on the population-level connectivity matrix through Burer-Monteiro factorization, which is well-suited for brain network analysis where connectivity patterns often exhibit inherent low-dimensional structure. Second, we enforce sparsity on the coefficient tensor using an L_0 constraint, reflecting the biological reality that covariate effects are typically confined to specific subsets of brain connections rather than affecting all edges uniformly. This sparsity assumption is crucial for interpretability in high-dimensional neuroimaging applications. Third, we developed an efficient Monte Carlo Expectation-Maximization (MCEM) algorithm to handle the computationally challenging optimization problem. The algorithm employs Metropolis-within-Gibbs sampling to approximate the intractable integrals in the E-step, while the M-step utilizes proximal gradient descent with hard thresholding to en-



(a) Axial and sagittal views of $\widehat{\mathcal{B}}_2$ and the corresponding functional region network.



(b) Axial and sagittal views of $\widehat{\mathcal{B}}_3$ and the corresponding functional region network.

Figure 6: Estimated $\widehat{\mathcal{B}}_2$ and $\widehat{\mathcal{B}}_3$ in Model 3. Red and blue edges indicate positive and negative entries in $\widehat{\mathcal{B}}_2$ and $\widehat{\mathcal{B}}_3$, respectively.

force the sparsity constraint on the coefficient tensor. The R code implementing our method is available at https://github.com/Zhentao20/MR_GLMM.

While our proposed method represents an advancement, there are several limitations that suggest directions for future research. Although our MCEM algorithm is more efficient than naive approaches, computational demands may become prohibitive for very large-scale networks (e.g., whole-brain analyses with thousands of ROIs). Future work could explore more efficient approximation schemes, such as variational inference methods or stochastic optimization algorithms that could handle larger network dimensions while maintaining statistical rigor. Moreover, modern neuroscience increasingly relies on multi-modal imaging approaches. Extending our framework to jointly model multiple types of connectivity data (e.g., structural and functional networks) or to incorporate additional data types (e.g., genetic information, behavioral measures) could provide more comprehensive insights into brain-behavior relationships.

7 Acknowledgment

Dr. Li’s research is partially supported by NIH grant R01-AG073259.

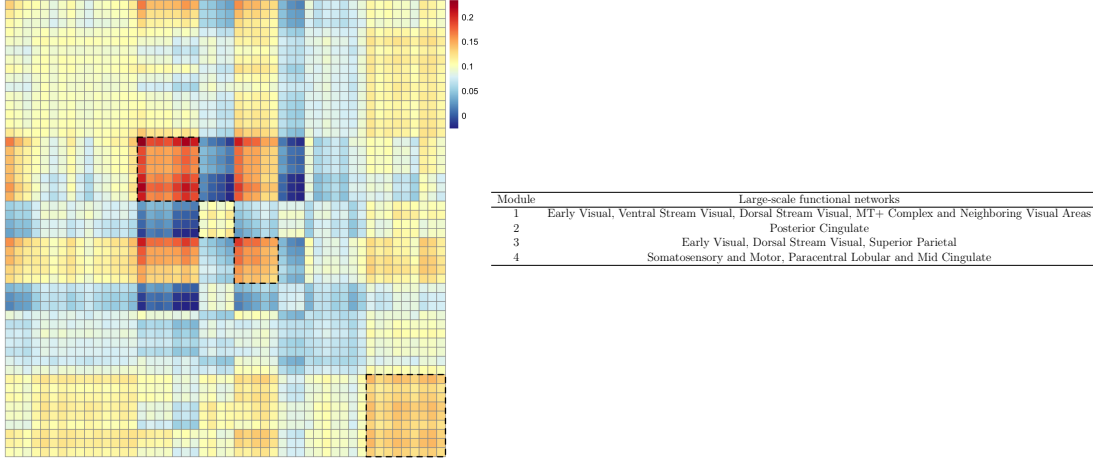
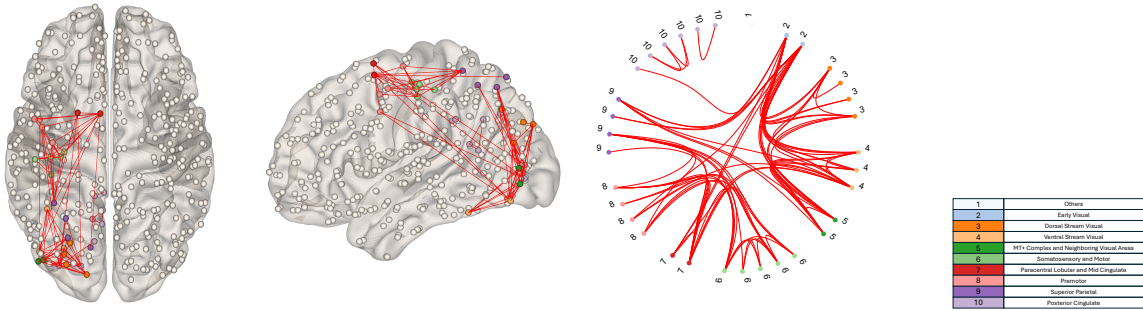


Figure 7: The heatmap of $\hat{\Theta}$, where rows and columns are arranged according to the K -means clustering. The black dashed lines represent the groups of functional modules identified in the clustering process with module names on the right table.



Axial and sagittal views of \hat{B}_1 and the corresponding functional region network. Red edges indicate positive entries in \hat{B}_1 .

Figure 8: Estimated \hat{B}_1 from the external validation dataset.

Appendix: Gradients Calculation

This appendix details the gradient calculations for the objective function $F(\boldsymbol{\vartheta})$ of linear and logistic models. For notational convenience, let

$$\mathbf{S} = \mathbf{U}^\top \mathbf{U} - \mathbf{V}^\top \mathbf{V}, \text{ where } S_{ks} = \sum_{a=1}^n (U_{ak} U_{as} - V_{ak} V_{as}).$$

Linear model. Define

$$\eta_{it,jj'}^{(m)} = (\mathbf{U}\mathbf{V}^\top)_{jj'} + \theta_{i,jj'}^{(m)} + \sum_{l=1}^p x_{itl} B_{jj'l}, \text{ and } r_{it,jj'}^{(m)} = A_{it,jj'} - \eta_{it,jj'}^{(m)},$$

where $\theta_{i,jj'}^{(m)}$ denotes the Monte Carlo samples as described in Section 3. Then, the elements of $\nabla F(\boldsymbol{\vartheta})$ are given by

$$\begin{aligned}\frac{\partial F}{\partial U_{j's}} &= -\frac{1}{M} \sum_{m=1}^M \sum_{i=1}^N \sum_{t=1}^{T_i} \sum_{j'=1}^n \frac{r_{it,jj'}^{(m)}}{\sigma_e^2} V_{j's} + 4\gamma \sum_{k=1}^r U_{jk} S_{ks}, \\ \frac{\partial F}{\partial V_{j's}} &= -\frac{1}{M} \sum_{m=1}^M \sum_{i=1}^N \sum_{t=1}^{T_i} \sum_{j'=1}^n \frac{r_{it,jj'}^{(m)}}{\sigma_e^2} U_{j's} - 4\gamma \sum_{k=1}^r V_{j'k} S_{ks}, \\ \frac{\partial F}{\partial B_{jj'l}} &= -\frac{1}{M} \sum_{m=1}^M \sum_{i=1}^N \sum_{t=1}^{T_i} \frac{r_{it,jj'}^{(m)}}{\sigma_e^2} x_{itl},\end{aligned}$$

Logistic model. Define

$$\eta_{it,jj'}^{(m)} = (\mathbf{UV}^\top)_{jj'} + \theta_{i,jj'}^{(m)} + \sum_{l=1}^p x_{itl} B_{jj'l}, \quad \pi_{it,jj'}^{(m)} = \frac{\exp(\eta_{it,jj'}^{(m)})}{1 + \exp(\eta_{it,jj'}^{(m)})}, \quad r_{it,jj'}^{(m)} = A_{it,jj'} - \pi_{it,jj'}^{(m)}.$$

where $\theta_{i,jj'}^{(m)}$ denotes the Monte Carlo samples as described in Section 3. Then, the elements of $\nabla F(\boldsymbol{\vartheta})$ are given by

$$\begin{aligned}\frac{\partial F}{\partial U_{j's}} &= -\frac{1}{M} \sum_{m=1}^M \sum_{i=1}^N \sum_{t=1}^{T_i} \sum_{j'=1}^n r_{it,jj'}^{(m)} V_{j's} + 4\gamma \sum_{k=1}^r U_{jk} S_{ks}, \\ \frac{\partial F}{\partial V_{j's}} &= -\frac{1}{M} \sum_{m=1}^M \sum_{i=1}^N \sum_{t=1}^{T_i} \sum_{j'=1}^n r_{it,jj'}^{(m)} U_{j's} - 4\gamma \sum_{k=1}^r V_{j'k} S_{ks}, \\ \frac{\partial F}{\partial B_{jj'l}} &= -\frac{1}{M} \sum_{m=1}^M \sum_{i=1}^N \sum_{t=1}^{T_i} r_{it,jj'}^{(m)} x_{itl}.\end{aligned}$$

References

- BABAEEGHAZVINI, P., RUEDA-DELGADO, L. M., GOOLJERS, J., SWINNEN, S. P. AND DAFFERTSHOFER, A. (2021). Brain structural and functional connectivity: A review of combined works of diffusion magnetic resonance imaging and electro-encephalography. *Frontiers in Human Neuroscience* **15**, 721206.
- BASSETT, D. S., ZURN, P. AND GOLD, J. I. (2018). On the nature and use of models in network neuroscience. *Nature Reviews Neuroscience* **19**, 566–578.
- BURER, S. AND MONTEIRO, R. D. C. (2003). A nonlinear programming algorithm for solving semidefinite programs via low-rank factorization. *Mathematical Programming* **95**(2), 329–357.

- CHEN, J. AND CHEN, Z. (2008). Extended bayesian information criteria for model selection with large model spaces. *Biometrika* **95**(3), 759–771.
- GILKS, W. R., BEST, N. G. AND TAN, K. K. C. (1995). Adaptive rejection metropolis sampling within gibbs sampling. *Journal of the Royal Statistical Society. Series C (Applied Statistics)* **44**(4), 455–472.
- HEILING, H. M., RASHID, N. U., LI, Q. AND IBRAHIM, J. G. (2024). glmmpen: High dimensional penalized generalized linear mixed models. *The R Journal* **15**(4), 106–128.
- HUI, F. K. C., MUELLER, S. AND WELSH, A. H. (2017). Joint selection in mixed models using regularized pql. *Journal of the American Statistical Association* **112**(519), 1323–1333.
- INGALHALIKAR, M., SMITH, A., PARKER, D., SATTERTHWAITE, T. D., ELLIOTT, M. A., RUPAREL, K., HAKONARSON, H., GUR, R. E., GUR, R. C. AND VERMA, R. (2014). Sex differences in the structural connectome of the human brain. *Proceedings of the National Academy of Sciences* **111**(2), 823–828.
- METROPOLIS, N., ROSENBLUTH, A. W., ROSENBLUTH, M. N., TELLER, A. H. AND TELLER, E. (1953). Equation of state calculations by fast computing machines. *The Journal of Chemical Physics* **21**(6), 1087–1092.
- PARIKH, N. AND BOYD, S. (2014). *Proximal algorithms*. Foundations and trends in Optimization. **1**, 127–239.
- ROUSSEEUW, P. J. (1987). Silhouettes: A graphical aid to the interpretation and validation of cluster analysis. *Journal of Computational and Applied Mathematics* **20**, 53–65.
- SMITH, S. M., BECKMANN, C. F., ANDERSSON, J., AUERBACH, E. J., BIJSTERBOSCH, J., DOUAUD, G., GLASSER, M. F., GROVES, E., JENKINSON, J., MOELLER, S., ROBINSON, S., SALIMI-KHORSHIDI, G., WOOLRICH, M. W., XU, J., YACOUB, E., UGURBIL, K. *and others*. (2013). Resting-state fmri in the human connectome project. *NeuroImage* **80**, 144–168.
- TOMASI, D. AND VOLKOW, N. D. (2012). Laterality patterns of brain functional connectivity density. *Proceedings of the National Academy of Sciences* **109**(20), E2287–E2296.
- VAN ESSEN, D. C., SMITH, S. M., BARCH, D. M., BEHRENS, T. E. J., YACOUB, E., UGURBIL, K. AND WU-MINN HCP CONSORTIUM. (2013). The Wu-Minn human connectome project: an overview. *NeuroImage* **80**, 62–79.
- ZHANG, J., SUN, W. W. AND LI, L. (2023). Generalized connectivity matrix response regression with applications in brain connectivity studies. *Journal of Computational and Graphical Statistics* **32**(1), 252–262.
- ZHAO, Y., CAFFO, B. S. AND LUO, X. (2024). Longitudinal regression of covariance matrix outcomes. *Biostatistics* **25**(2), 385–401.

ZHOU, Y. AND MUELLER, H. G. (2022). Network regression with graph laplacians.
Journal of Machine Learning Research **23**(320), 1–41.